Pharm Res (2012) 29:3312–3324
DOI 10.1007/s11095-012-0823-4

RESEARCH PAPER

Mechanisms of Tumor Vascular Priming by a Nanoparticulate Doxorubicin Formulation

Tista Roy Chaudhuri • Robert D. Arnold • Jun Yang • Steven G. Turowski • Yang Qu • Joseph A. Spernyak • Richard Mazurchuk • Donald E. Mager • Robert M. Straubinger

Received: 30 March 2012 / Accepted: 25 June 2012 / Published online: 14 July 2012

ABSTRACT

Purpose Tumor vascular normalization by antiangiogenic agents may increase tumor perfusion but reestablish vascular barrier properties in CNS tumors. Vascular priming *via* nanoparticulate carriers represents a mechanistically distinct alternative. This study investigated mechanisms by which sterically-stabilized liposomal doxorubicin (SSL-DXR) modulates tumor vascular properties.

Methods Functional vascular responses to SSL-DXR were investigated in orthotopic rat brain tumors using deposition of fluorescent permeability probes and dynamic contrast-enhanced magnetic resonance imaging. Microvessel density and tumor burden were quantified by immunohistochemistry (CD-31) and quantitative RT-PCR (VE-cadherin).

Results Administration of SSL-DXR (5.7 mg/kg *iv*) initially (3–4 days post-treatment) decreased tumor vascular permeability, k_{trans} (vascular exchange constant), vascular endothelial cell content, microvessel density, and deposition of nanoparticulates. Tumor vasculature became less chaotic. Permeability and perfusion returned to control values 6–7 days post-treatment, but intratumor SSL-DXR depot continued to effect tumor vascular endothelial compartment 7–10 days post-treatment, mediating enhanced permeability.

Conclusions SSL-DXR ultimately increased tumor vascular permeability, but initially normalized tumor vasculature and decreased tumor perfusion, permeability, and nanoparticulate deposition. These temporal changes in vascular integrity resulting from a single SSL-DXR dose have important implications for the design of combination therapies incorporating nanoparticle-based agents for tumor vascular priming.

KEY WORDS brain tumors · nanoparticulate drug carriers · sterically-stabilized liposomes · tumor priming · tumor vascular permeability

ABBREVIATIONS

DCE-MRI	dynamic contrast-enhanced magnetic resonance imaging
dNTP	deoxynucleotide triphosphate
DSPC	distearoylphosphatidylcholine
DXR	doxorubicin
eGFP	enhanced green fluorescent protein
PEG-DSPE	distereoylphosphatidylethanolamine derivatized with polyethylene glycol
PK	pharmacokinetic
qRT-PCR	quantitative reverse transcriptase—polymerase chain reaction
SSL	sterically stabilized liposomes
SSL-DXR	sterically stabilized liposomes containing doxorubicin

INTRODUCTION

Malignant brain tumors are relatively rare but highly fatal. Approximately 60% of the 22,000 patients diagnosed annually with brain/CNS cancers succumb (1). Brain tumors cause 26% of cancer deaths in children, and are second only to leukemia in incidence (2,3). Duration of remission and survival has increased for numerous cancers, but primary

T. Roy Chaudhuri • R. D. Arnold • J. Yang • Y. Qu • D. E. Mager • R. M. Straubinger (✉)
Department of Pharmaceutical Sciences
University at Buffalo, State University of New York
445 Kapoor Hall, Buffalo, New York 14214-8033, USA
e-mail: rms@Buffalo.edu

T. Roy Chaudhuri • S. G. Turowski • J. A. Spernyak • R. Mazurchuk • R. M. Straubinger
Department of Molecular and Cellular Biophysics and Biochemistry
Roswell Park Cancer Institute
Elm/Carlton Streets, Buffalo, New York 14263, USA

and metastatic brain tumors were as lethal in the 2000's as in the 1970's (4).

Malignant brain tumors are among the most therapeutically challenging solid tumors, with frequent recurrence within several cm of the resection site (5). Tumor may be shielded from systemic chemotherapy by poorly-functioning vasculature and high interstitial pressure, which results in low drug deposition (6–9). Standard care includes chemotherapy and radiotherapy in order to eliminate local extensions of metastatic tumor that remain following surgery (3,10,11). Median survival of malignant gliomas treated by surgery, surgery/radiation or surgery/chemotherapy was 14, 20, and 40–50 weeks, respectively (11).

Strategies to improve drug delivery could increase the efficacy of brain tumor therapy, and nanoparticulate drug carriers have the potential to overcome several factors that limit therapeutic success. Renal clearance is reduced progressively as carrier diameter increases >6–10 nm, thereby extending drug circulation lifetime and systemic exposure considerably (12,13). Confinement of carrier-encapsulated drugs to the vasculature reduces their volume of distribution and access to critical normal tissues, permitting higher doses and potentially overcoming functional resistance (14). Provided the carrier diameter is <100–120 nm and other physical properties are appropriate (15–20), circulation half-life for some carriers can be prolonged to 24–36 h (21,22). Long-circulating particulate carriers are able to extravasate through the flawed tumor microvasculature and increase drug deposition *via* the enhanced permeability and retention phenomenon (EPR) that arises because of rapid, chaotic tumor vascular growth, dysregulated vasculogenesis, and vascular barrier compromise (13,23–25). Several carrier types have a high cargo capacity and can convey large quantities of drug to tumors. Thus nanoparticulate carriers represent an important strategy to exploit tumor physiology and architecture to improve efficacy.

The pharmacology of drugs encapsulated in particulate carriers may be altered significantly compared to the unencapsulated free drug (21,22). An example is the clinically-approved product Doxil®, a sterically-stabilized liposome (SSL) formulation containing doxorubicin (DXR) gelled in semi-crystalline form in the interior of 65–80 nm liposomes (26–28). We observed previously that weekly administration of SSL-DXR resulted in a significant increase in lifespan of rats bearing intracranial brain tumors, whereas free DXR was ineffective (24). Furthermore, tumor deposition of SSL-DXR more than doubled if the animals had received a dose of SSL-DXR one week prior (25), and disseminated microhemorrhage within tumors increased in incidence after the 2nd and 3rd weekly doses (23). Evaluations of intratumor SSL-DXR distribution suggest that following extravasation, relatively little tumor penetration occurs (24,29), implicating perivascular accumulation as a primary mechanism underlying tumor antivascular effects.

Vascular compromise and enhanced deposition of subsequently-administered drugs has been demonstrated with SSL formulations containing several different drugs (30,31). Therefore, given the generalizability of these 'tumor priming' effects of carrier-encapsulated drugs, we investigated the sequence of events that occur in treatment-naïve tumors following administration of SSL-DXR, using an orthotopic rat model of invasive brain cancer. Dynamic contrast-enhanced (DCE) magnetic resonance imaging (MRI) was used to monitor the functional status of tumor vasculature, and a population-based pharmacokinetic (PK) approach was employed to estimate tumor vascular permeability and perfusion (32,33) from the data. Immunohistological analysis and intratumor deposition of *iv* injected probes of vascular permeability were employed to examine SSL-DXR treatment effects upon morphology and functionality of tumor vasculature.

MATERIALS AND METHODS

Materials

Doxorubicin-HCl and cholesterol were from Sigma (St. Louis, MO). Distearoylphosphatidylcholine (DSPC) and distereoylphosphatidylethanolamine conjugated with 1900 Da polyethylene glycol (PEG-DSPE) were from Avanti Polar Lipids (Alabaster, AL). Dioctadecyl-3,3,3′,3′-tetramethylindocarbocyanine disulfonate ($DiIC_{18}$(5)-DS) was from Invitrogen Inc. (Carlsbad, CA). The 9L cell line designated 9L-72 was obtained from Dr. Dennis Deen of the University of California/San Francisco. A stable clonally-selected 9L cell line expressing enhanced green fluorescence protein (9L-eGFP) was developed by transducing parental 9L cells with a retroviral vector driving constitutive eGFP expression under a cytomegalovirus promoter.

R. M. Straubinger
New York State Center of Excellence in Bioinformatics and Life Sciences
701 Ellicott St., Buffalo, New York 14203-1101, USA

Present Address:
R. D. Arnold
Department of Pharmacal, Harrison School of Pharmacy
Auburn University, Auburn, A 36849-5504, USA

Present Address:
R. Mazurchuk
Division of Cancer Prevention, National Cancer Institute
Executive Plaza North, Ste. 3100, 6130 Executive Blvd., MSC 7362
Bethesda, Maryland 20892-7362, USA

Methods

Preparation of SSL-DXR

The remote loading drug encapsulation procedure used by our lab is described in detail (24,25,34,35). Additional publications describe the general principles and applications of the procedure (26–28,36–38). Briefly, a thin film of DSPC:cholesterol: PEG-DSPE (9:5:1 mol ratio) was hydrated with 250 mM ammonium sulfate, extruded multiple times through polycarbonate filters (GE Water & Process Technologies, Trevose, PA) of successively decreasing pore sizes to a final diameter of 80 nm, dialyzed against isotonic sucrose, and then loaded with DXR HCl (10.5 mg/ml, pH 6.4) at 60°C for 1 h at a drug:lipid ratio of 0.25:1. The final particle diameter as determined by quasi-elastic light scattering was 85–110 nm. After removal of any unencapsulated DXR by dialysis, phospholipid content was measured (39) and encapsulated drug was measured by absorbance in acidified ethanol. Typically 95–100% of the drug was encapsulated.

Tumor Implantation and Treatment

Except where noted, 9L tumor cells were grown as spheroids in Dulbecco modified Eagle medium/Ham's F-12 medium containing 20 ng/mL basic fibroblast growth factor, 20 ng/mL epidermal growth factor, 50 ng/mL heparin, and 1x B-27 nutrient supplement (40) (Invitrogen). Under these conditions, Nestin and Sox2 are up-regulated, and spheroid-derived tumors are more rapidly growing, aggressive, and drug resistant (40).

Intracranial 9L tumors were established by stereotaxic injection of 4×10^4 cells in 4 μL into the caudate-putamen region of 180–200 g male Fisher 344 rats (Harlan Sprague Dawley, Indianapolis, IN) (23,24). When intracranial tumors were well-established, a single dose of SSL-DXR (5.7 mg/kg) was administered *iv* by tail vein injection. For DCE-MRI studies, tumors were measured by MR imaging and SSL-DXR was administered when tumors reached 3–5 mm^3 (7–9 days after implantation). For qRT-PCR and immunohistological/fluorescence experiments, tumors were not staged by MRI, and all animals were treated 7 days after implantation.

DCE-MR Imaging

MR imaging employed a 4.7 Tesla GE system (Fremont, CA) incorporating AVANCE digital electronics and ParaVision 3.0.2 acquisition software (Brüker Medical, Billerica, MA). A custom-built 45 mm (ID) radiofrequency transceiver coil (Insight Neuroimaging Systems, Worcester, MA) was used for acquiring DCE imaging data sets. Prior to imaging, a catheter was inserted into the lateral tail vein for administration of the contrast agent. Animals (n=8–10 per treatment group) were anesthetized with isoflurane, and body temperature and respiration were monitored continuously while imaging.

Following scout scans, a multi-slice, T2-weighted fast spin echo scan was acquired for tumor volume measurement with the following parameters: trans-axial orientation; field of view (FOV)=4.5×4.5 cm; slice thickness=1 mm; matrix size=192×192; effective echo time (TE)=60 ms; repetition time (TR)=3200 ms; echo train length=8; number of averages (NEX)=6. For DCE-imaging, a single 1.5 mm thick slice with the identical FOV was prescribed through the center of the tumor. Baseline T1 relaxation rates were measured using an inversion-recovery TrueFISP acquisition (41) with the following parameters: matrix size=128×128, TE/TR=1.5/3.0 ms, flip angle=30°, inversion repetition time=10 s, segments=16, frames=50. Total acquisition time for each T1 measurement was 160 s. Following acquisition of baseline T1 values, Gd-DTPA (diethylenetriamine pentaacetate chelate of gadolinium; Bayer HealthCare Inc., Wayne, NJ) was infused over 7.5 min using a pump. The total dose was 0.3 mmol Gd^{3+}/kg. T1 measurements were acquired serially for 50 min after initiation of Gd-DTPA administration.

Image Processing and Analysis

Regions of interest (ROI) capturing the tumor and superficial temporal veins were created for each data set using Analyze 7.0 (Analyze Direct, Overland Park, KS). Signal intensities were extracted from each ROI, and T1 relaxation rates were calculated according to (41) using routines developed in-house with MATLAB (Mathworks, Natick, MA). The concentration of Gd-DTPA ($[C_t]$) at time t was calculated as:

$$C_t = \frac{R1_t - R1_0}{r1}$$

where $R1_t$ is the T1 relaxation rate at t, $R1_0$ is the baseline relaxation rate, and $r1$ is the T1 relaxivity of Gd-DTPA, measured as 3.1 $(mM{\bullet}s)^{-1}$ at 4.7T, 37°C.

The area-under-the-curve (AUC) of Gd-DTPA in the tumor ROI was calculated using the trapezoidal rule:

$$AUC_{0-50\ min} = \sum_{n=0}^{50\ min} \frac{(C_n + C_{n+1})}{2}(t_{n+1} - t_n)$$

where C_n is the concentration of Gd-DTPA at time t_n.

A two-compartment population PK model was used to estimate the first-order transfer coefficient of contrast enhancing agent from plasma into the tumor interstitium (k_{trans}) and the fraction of extracellular volume of tumor

(v_e).[1] The model employed a nonlinear mixed effects approach implemented in NONMEM 5.1.1 (University of California, San Francisco, CA). Statistical analysis was performed using S-PLUS 7.0 (Insightful Corp., Seattle, WA).

Quantification of Vascular Endothelium Content by qRT-PCR

To provide a quantifiable marker for tumor cell burden in the harvested tissue, 9L tumor cells were mixed in a 2:1 ratio with 9L-eGFP cells before implantation so that tumor growth characteristics remained the same for all experiments. Animals were treated 7 days after implantation with 5.7 mg/kg of SSL-DXR or saline (control), and n=3–5 animals per treatment group were sacrificed on days 2, 4, 7, 9 and 11 after treatment. The brain was removed, bisected, and the tumor was identified visually and excised. A sample of normal brain was taken from the same region of the contralateral hemisphere. The tissue was frozen rapidly in liquid nitrogen.

The frozen tissue samples were weighed and ground under liquid nitrogen using a mortar and pestle. Total RNA was extracted and purified using a kit (SV Total, Promega, Inc., Madison, WI). The yield and quality of RNA was determined by absorbance ratios at 260/280 (1.7–2.1) and 260/230 (1.8–2.2). For cDNA synthesis, mRNA was incubated with 500 ng oligo$(dT)_{12–18}$ at 65°C for 5 min and then cooled to room temperature. The 10x first-strand buffer, dNTP mixture (1 mM each), RNaseOUT (40 units, Invitrogen) and StrataScript reverse transcriptase (50 units, Agilent, Santa Clara, CA) were incubated together for 1 h at 42°C. The reaction was stopped by heating (90°C for 5 min).

The resulting cDNAs were subjected to PCR quantification of a variety of markers for tumor burden and vasculogenesis. Markers for vascular endothelial cell content (VE-cadherin and PECAM-1) (42) changed significantly with SSL-DXR treatment and are reported here. Amplicon length and forward/reverse primers were: eGFP (206 bp, CTTCTTCAAGTCCGCCATGC/AGACGTTGTGGCTGTTGTAG); VE-cadherin (126 bp, TGCCCTCATTGTGGACAAGAA/GGCACAGATGCGTTGAATAC); PECAM-1 (140 bp, CAGCAGGCATCGGCAAA/TGACTGGCAGCTGATACCTATGAT). The data were normalized against β actin (81 bp, AGCCATGTACGTAGCCATCCA/TCTCCGGAGTCCATCACAATG), Cyclophilin A (94 bp, CCAAACACAAATGGTTCCCAGTT/TGCCTTCTTTCACCTTCCCAAA), and GAPDH (191 bp, AACGACCCCTTCATTGAC/TCCACGACATACTCAGCAC) (43).

For each marker, relative measures of gene expression were determined using 50 µl reactions containing 1.5 mM $MgCl_2$, 0.5 µM primer, 200 µM dNTP, 0.5 µl SYBR Green (1/750 dilution) and 0.5 µl 5-carboxy-X-rhodamine (ROX) dye (1/500 dilution), and 1U MasterTaq DNA polymerase (Promega). The thermocycle consisted of 95°C (5 min), followed by 40 cycles of: 95°C (30 s); 60°C (30 s); 72°C (30 s). Dissociation curve- and electrophoretic analysis confirmed the presence of a single PCR product. Normalization was based upon the geometric mean of the control gene panel, and the gene-stability measure (43) was calculated for all pairwise combinations of control genes using routines implemented in-house in MATLAB.

Vascular Permeability

Fluorescently-labeled SSL equivalent in size to SSL-DXR contained 0.1 mole% $DiIC_{18}(5)$-DS, a non-exchangeable liposome membrane label (44,45) (DiI-SSL), and were used to probe tumor vascular permeability and intratumor disposition. On day 3 or 6 after treatment of tumor bearing rats with SSL-DXR or saline (control), DiI-SSL (approx. 7 µmol phospholipid) were injected *iv*, and after 24 h, 3 animals per treatment group were exsanguinated by flushing the vasculature with heparinized saline and the brain was extracted. The tumor-bearing and contralateral hemispheres were separated and embedded in OCT (Tissue-tek, Sakura Finetek, Torrance, CA) and frozen rapidly in liquid propane over liquid nitrogen. Frozen sections (10 µm) were cut for fluorescence and immunohistochemical evaluation.

A fluorescence microscope (Axiovert 200 M; Carl Zeiss, Inc, Thornwood, NY) was used to image $DiIC_{18}(5)$-DS, using filter set #50 (excitation 640 nm, emission 690). Panoramas encompassing the entire tumor were acquired under computer control using constant exposure conditions (100 ms exposure, digital gain 2) and a 20X/0.75 Apochromat objective lens.

Microvessel Density

Slide-mounted sections were fixed with ice-cold acetone, washed with phosphate buffered saline (PBS)/0.5% Tween 20, incubated in 3% H_2O_2 in water to inactivate endogenous peroxidases, and blocked with 6% FBS in PBS. Sections were incubated with 2 µg/ml mouse anti-rat CD31 (Chemicon, Billerica, MA) for 1 h at 20°C, washed with PBS, incubated for 30 min with 2 µg/ml biotinylated rat anti-mouse IgG (Vector Laboratories, Burlingame, CA), washed, and visualized using diaminobenzidine.

[1] Yang J, Roy Chaudhuri T, Mager DE, Spernyak JA, Straubinger RM. Application of nonlinear mixed effects analysis to dynamic contrast enhanced magnetic resonance imaging in a rat brain tumor model. Unpublished 2011.

Statistical Analysis

A single-tailed Student *t*-test was used for comparison of treatment and control groups using Prism5.0d (Graphpad Software, La Jolla, CA).

RESULTS

Previously we demonstrated that repetitive treatment of rats bearing intracranial 9L tumors at 7-day intervals with SSL-DXR, but not free DXR, resulted in progressive tumor vascular barrier compromise, increased tumor deposition of subsequent SSL-DXR doses, and significant extension of lifespan (23–25). SSL-DXR at 5.7 mg/kg administered *iv* weekly for 3 weeks was the maximally-efficacious and maximum-tolerated dose (24). An equivalent regimen of free DXR lacked efficacy and showed delayed, lethal toxicity. Given the lack of insight as to how incorporation of DXR into nanoparticles alters the functional pharmacology of the encapsulated agent, we investigated the temporal effects mediated by a single dose of SSL-DXR in treatment-naïve animals.

Tumor Vascular Perfusion and Permeability

DCE-MRI was employed for noninvasive assessment of SSL-DXR effects upon tumor vascular permeability and perfusion. One day after *iv* administration of 5.7 mg/kg SSL-DXR, there was no effect upon tumor vascular permeability/perfusion. However, 3 days after treatment, both the rate of Gd-DTPA deposition in intracranial tumors (Fig. 1a) and tumor exposure (AUC) (Fig. 1b) were reduced significantly ($P<0.05$) compared to saline-treated control animals. No changes in Gd-DTPA uptake or AUC were observed in normal brain or other tissues (not shown).

Five or 7 days after SSL-DXR treatment, tumor vascular perfusion and permeability recovered, and the AUC of Gd-DTPA was nearly equal in both groups (Fig. 1b). Previously we observed that 7 days after an SSL-DXR dose, residual DXR concentrations in tumor exceeded the peak concentration achieved after bolus administration of free DXR, and tumor deposition of SSL-DXR administered 7 days after the initial SSL-DXR dose increased two-fold (25). Thus the residual intratumor drug reservoir may continue to erode vascular integrity a week after dosing, and as permeability/perfusion recovers in SSL-DXR-treated animals, a crossover point may exist approx. 7–9 days post-dosing that marks a transition from reduced tumor vascular perfusion/permeability to elevated permeability to nanoparticles.

The tumor:vascular fluid exchange parameter (k_{trans}) and the volume fraction of tumor perfused by Gd-DTPA (v_e) were determined by applying a population-based PK model to the DCE-MRI data. Both k_{trans} (Fig. 1c) and v_e (Fig. 1d) increased in control animals as tumor volume increased. However, consistent with tumor perfusion data following SSL-DXR treatment, k_{trans} and v_e were suppressed significantly compared to controls ($P<0.01$) on day 3 after the single SSL-DXR dose.

Permeability to Nanoparticulates

DCE-MRI data suggested that the initial effect of SSL-DXR was a reduction in tumor vascular perfusion/permeability. To investigate SSL-DXR effects upon vascular integrity and permeability to nanoparticle drug carriers, control- and SSL-DXR-treated animals were injected *iv* with fluorescent 85–110 nm SSL (DiI-SSL) at various times after treatment. Animals were sacrificed 24 h later, the time of peak SSL deposition (25). In control animals, tumors displayed sporadic and highly intense fluorescence accumulations (Fig. 2a). In contrast, at the same time point 3 days after SSL-DXR treatment, animals showed fewer intense fluorescence accretions (Fig. 2b). Seven days after SSL-DXR treatment, tumor deposition of probe SSL-DiI was similar in control (Fig. 2c) and treated (Fig. 2d) animals.

Deposition of DiI-SSL was quantified in both the peripheral invasive region and the less vascularized tumor core. In animals receiving probe liposomes 3 days after SSL-DXR treatment, DiI-SSL deposition 24 h later was significantly lower in both the tumor core ($P<0.05$; Fig. 3a) and invasive margin ($P<0.01$; Fig. 3b) of treated animals compared to controls. DiI-SSL deposition was equivalent in the two groups when probe liposomes were administered 6 days after treatment, but was lower for both groups compared to deposition probed 3 days after SSL-DXR administration. The lower deposition on day 6 compared to day 3 was significant in the tumor core ($P<0.001$; Fig. 3a), suggesting declining vascular function as the tumor expanded within the confines of the brain and tumor cellular density increased.

The uniformity of DiI-SSL deposition was quantified to investigate the apparent shift in deposition from fewer, larger fluorescence accretions in controls (Fig. 2a) to more numerous, less intense structures in SSL-DXR-treated animals (Fig. 2b). To accomplish this, the tumor region was divided into a grid of small sub-regions. Mean fluorescence in each sub-region was quantified and the variability among sub-regions was calculated. Animals treated with a single dose of SSL-DXR had a significantly lower variance in mean deposition of DiI-SSL compared to controls ($P<0.05$) when the DiI-SSL were injected 3 days after treatment (Fig. 3c), supporting quantitatively the greater apparent uniformity of deposition following SSL-DXR treatment. When vascular permeability was probed with DiI-SSL 6 days after SSL-DXR, the variance in DiI-SSL deposition did not differ between treated and control animals.

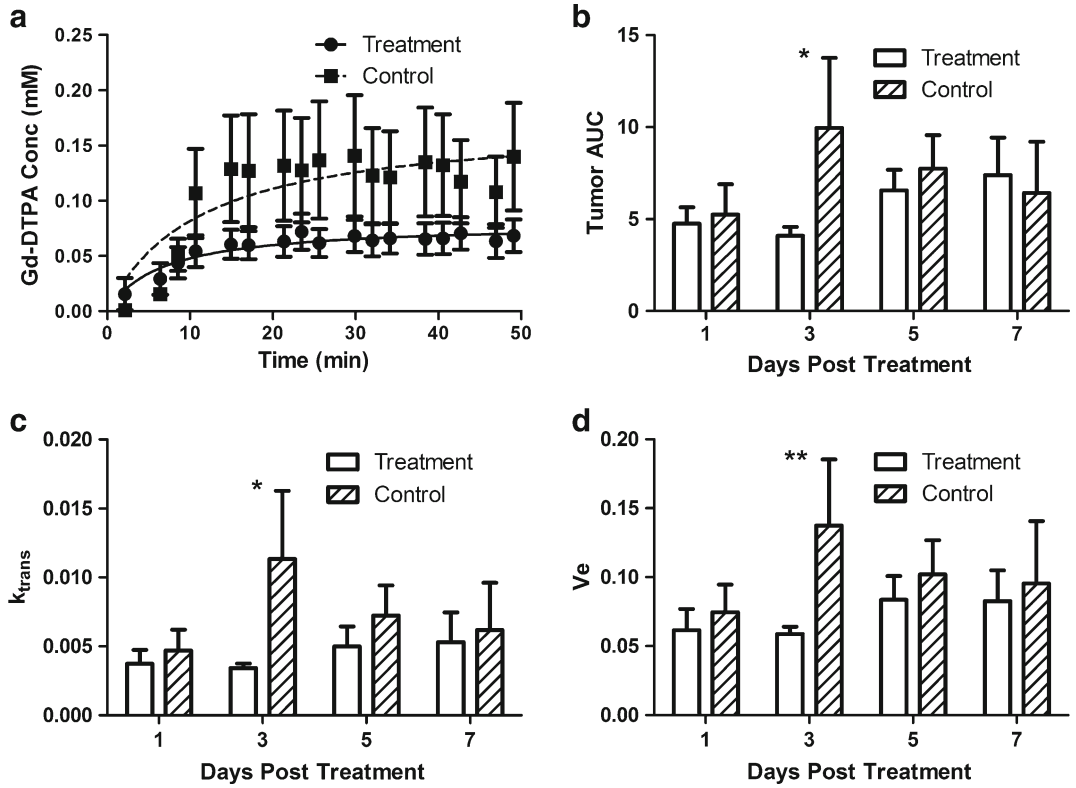

Fig. 1 Temporal effects of SSL-DXR administration on intracranial 9L tumor vascular perfusion and permeability. Fisher 344 male rats (n=8–10/treatment group) bearing intracranial 9L tumors were treated *iv* with a single dose of SSL-DXR (5.7 mg DXR/kg) when tumors reached a volume of 3–5 mm^3 (7–9 days after implantation). Controls received saline. Tumor volume was estimated from high-resolution T2-weighted images and DCE-MRI with Gd-DTPA contrast agent was performed for vascular permeability and perfusion measurements. T1 relaxation rate measurements were acquired before, during, and after Gd-DTPA infusion. (**a**) Tumor concentration-time profile of Gd-DTPA 3 days after SSL-DXR (circles, solid line) or saline (squares, dashed line) treatment. Concentration of Gd-DTPA was determined from T1 relaxation rates (*Methods*). Lines through the data represent the best fit of the Michaelis-Menten equation. (**b**) Gd-DTPA exposure of treated *vs.* control tumors on different days after SSL-DXR treatment. Open bars: SSL-DXR-treated animals; hatched bars: control animals. Ordinate: $AUC_{0\text{-}50}$ (area under Gd-DTPA concentration-time curve) determined for the 50 min following infusion. The 2-fold reduction in AUC for SSL-DXR-treated animals was significant (*, $P<0.05$) on day 3. (**c**) The tumor:vasculature exchange constant k_{trans} was calculated for Gd-DTPA using a population PK model (*Methods*). The 3-fold lower value of k_{trans} in treated animals differed significantly (*, $P<0.05$) from controls on day 3. (**d**) v_e (extracellular volume available to Gd-DTPA) was significantly (**, $P<0.01$) lower on day 3 in tumors of treated animals compared to controls.

Microvessel Density

The treatment-mediated changes in the quantity and pattern of DiI-SSL deposition mediated by SSL-DXR treatment suggested effects upon the pattern and density of tumor microvasculature in SSL-DXR-treated animals (Fig. 2b). Microvessel density and morphology were therefore evaluated. Immunohistochemical staining of CD31-positive structures showed chaotic and disorganized vasculature in control animals on the day that would be equivalent to day 4 post-SSL-DXR (Fig. 4a). In contrast, numerous densely-stained, vessel-like structures were observed throughout the tumor 4 days after animals were treated with SSL-DXR (Fig. 4b).

Treatment effects upon tumor microvessel density were quantified. On day 4 after treatment, the density of CD31-stained elements was significantly lower ($P<0.0001$) in treated animals than in controls evaluated on the equivalent day (Table 1). On day 7 post-treatment, the density of CD31-stained structures had increased significantly ($P<0.001$) in animals treated with SSL-DXR, suggesting rebound expansion of the tumor vasculature (Table 1). Treated and control groups did not differ significantly from each other on day 7.

Effect of SSL-DXR Treatment on Tumor Microvessel Content

Responses to a single SSL-DXR treatment suggested a clear temporal pattern of effects upon tumor vascular permeability and perfusion, as well as on microvessel density and organization. The magnitude and time course of SSL-DXR treatment effects upon vasculature were evaluated by qRT-PCR using a panel of vasculogenesis-related markers. Intracranial 9L tumors are unencapsulated and invasive. In order to quantify tumor burden in tissue samples, the initial tumor cell inoculum of parental 9L tumor cells included a constant proportion of 9L cells constitutively

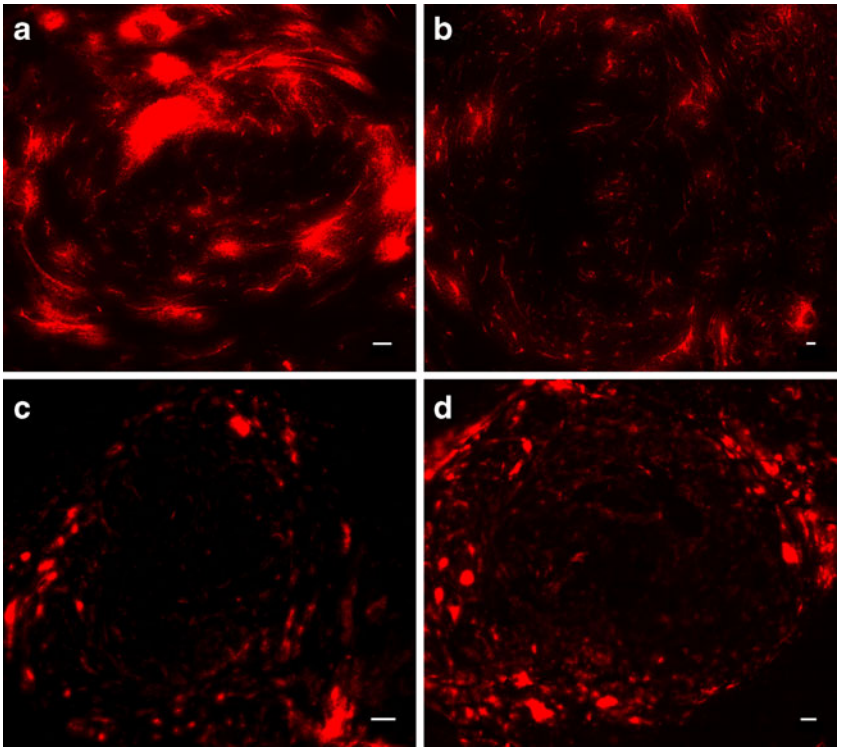

Fig. 2 Effect of single SSL-DXR treatment on permeability of intracranial 9L tumors to fluorescently-labeled sterically-stabilized liposomes. Three and 6 days after treatment with SSL-DXR, animals were injected *iv* with 85–110 nm SSL labeled with 0.1 mole% of the non-exchangeable fluorophore $DiIC_{18}(5)$-DS and sacrificed at 24 h. The brain was rapidly removed, frozen, and 10 μm sections were cut. Panoramas encompassing the entire tumor region were acquired using constant exposure conditions (*Methods*). (**a**) Tumors of saline-treated controls or (**b**) SSL-DXR-treated animals injected *iv* with fluorescent SSL 3 days after treatment and imaged 1 day later. Accretions of fluorescent DiI-SSL in tumors of SSL-DXR-treated animals were smaller and less numerous than in control animals, but contained a larger number of strand-like features resembling perfused vessels. (**c**) Tumors of controls or (**d**) treated animals injected *iv* with DiI-SSL 6 days after SSL-DXR treatment and imaged 1 day later. The tumor core of both control- and treated animals showed decreased overall DiI-SSL deposition on day 6–7 compared to day 3–4, but were similar to each other. Bar: 50 μm. Image intensity in (**c**) and (**d**) was increased to reveal patterns of deposition.

expressing eGFP (9L-eGFP) to permit visualization and quantification of tumor cell content.

At intervals over 2 weeks following a single SSL-DXR treatment, groups of 3–5 treated and control animals were sacrificed at each time point. The brain region containing the tumor was identified visually and excised, as was normal brain from the contralateral hemisphere.

For most angiogenesis-related markers in the panel, there was no significant difference between treated- and control groups over the time period surveyed (data not shown). However, markers for vascular endothelium content differed consistently. Tumor content of VE-cadherin (Fig. 5a) rose progressively over a week of observation in the tumors of control rats, confirming the rapid expansion of the vascular compartment suggested by DCE-MRI (Fig. 1). Notably, a single dose of SSL-DXR abolished the vascular endothelium expansion (Fig. 5a), and the difference was significant ($P< 0.05$) 7 days after treatment.

Based on 9L-eGFP abundance in the tumor sample, tumor cell density remained relatively constant over the first week after SSL-DXR treatment (Fig. 5b). In the second week, tumor cell density rose precipitously in both groups, and the single SSL-DXR treatment did not have a discernible effect on tumor progression.

The temporal changes in vascular endothelial cell content (Fig. 5a) and tumor cell burden (Fig. 5b) appeared to be correlated. Therefore the VE-cadherin:eGFP ratio for each individual animal was calculated as an indicator of the microvessel content of tumor (Fig. 5c). Over the first week of evaluation, the endothelium:tumor cell ratio rose rapidly in control animals. The nearly 7-fold elevation in that ratio for control animals on day 7 after treatment was significantly higher than in SSL-DXR-treated animals ($P<0.05$), and the effect of a single SSL-DXR treatment on the endothelium:tumor cell ratio was striking. After approx. 7 days, tumor cell density increased rapidly (Fig. 5b), causing a rapid decline in the VE-cadherin:eGFP ratio (Fig. 5c). Overall, the data suggest that the initial, rapid expansion of tumor microvasculature primed the tumor for rapid growth and increasingly dense cellularity, and the single SSL-DXR dose eliminated the expansion of the vascular endothelial cell compartment.

Data for PECAM-1, a second marker of vascular endothelial content of tissue (42), was consistent with the data for

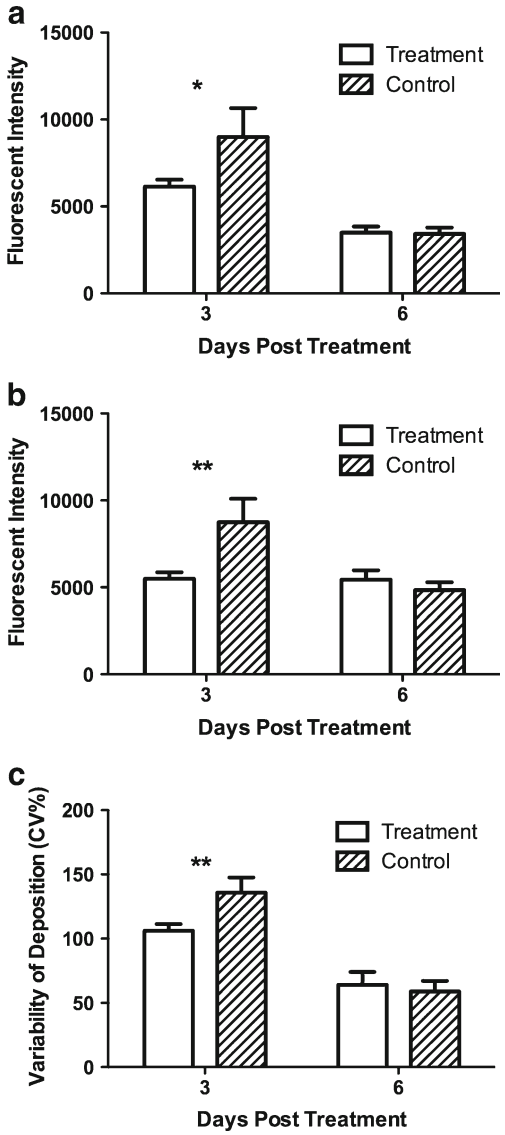

Fig. 3 Quantification of SSL-DXR effects on intracranial 9L tumor vascular permeability to sterically-stabilized probe liposomes. Tumor deposition of fluorescent DiI-SSL was quantified from images of 10 μm frozen tissue sections encompassing the entire tumor of control- and SSL-DXR-treated animals (*cf.* Fig. 2) using *ImageJ*. (**a**) Deposition of DiI-SSL in the tumor core region of SSL-treated- (open bars) or control (hatched bars) animals. Ordinate: arbitrary fluorescence units per unit area over equal-sized regions-of-interest (ROI). The difference between SSL-DXR-treated and control groups was significant for animals injected on day 3 post treatment with DiI-SSL (*, $P<0.05$), but not in animals probed on day 6 after treatment. (**b**) Deposition of DiI-SSL in the invasive peripheral tumor region at varying times after SSL-DXR treatment. The difference between SSL-DXR-treated and control animals was significant for animals injected on day 3 post treatment with DiI-SSL (**, $P<0.01$), but not on day 6. (**c**) The uniformity of intratumor deposition of DiI-SSL was quantified for animals injected with the probe liposomes on day 3 or 6 after SSL-DXR treatment or control (saline) administration (*Methods*). A higher variability of fluorescence (ordinate) indicates less uniform deposition in the control group. SSL-DXR treatment reduced the covariance of fluorescent intensity significantly (**, $P<0.01$), indicating more uniform intratumor deposition.

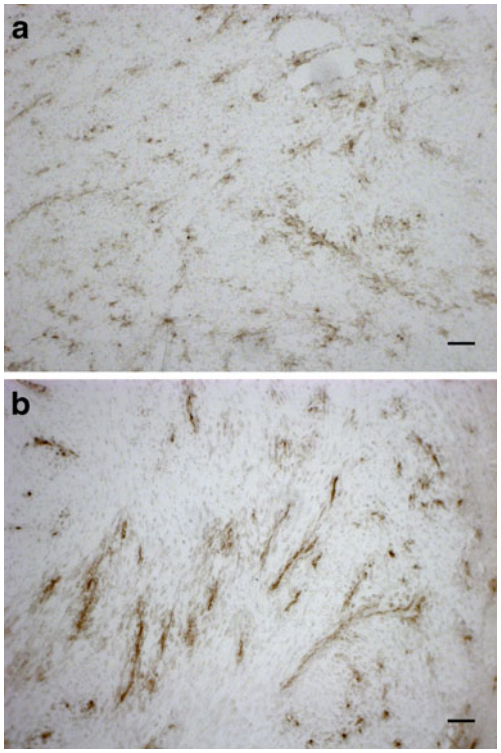

Fig. 4 Changes in tumor microvessel density and morphology mediated by SSL-DXR. Microvessel density and morphology were evaluated by CD31 immunostaining of frozen tumor sections obtained at the same times that tumor vasculature was probed for permeability (*cf.* Figs. 2 and 3). (**a**) Control animals showed chaotic, disorganized tumor microvasculature 4 days after saline treatment. (**b**) SSL-DXR-treated animals showed fewer but larger organized, intensely-staining CD31-positive structures 4 days after treatment. Bar represents 50 μm.

VE-cadherin. However, because of variability in the data when normalized by control genes, which are present both in tumor and any residual normal brain tissue included in the sample, the reduction in PECAM-1 abundance in tumors of treated *vs.* control animals did not rise to statistical significance (not shown). However, with normalization of PECAM-1 data by the tumor cell content (eGFP) of the sample for each individual animal (*cf.* Fig. 5c), suppression of PECAM-1 by the SSL-DXR treatment rose to statistical

Table 1 Mean Tumor Microvessel Density

Days Post Treatment	Control [a]	(n [b])	SSL-DXR [a]	(n [b])	*p*
4	87.9 ± 2.8	(41)	60.8 ± 1.7	(29)	<0.0001
7	91.1 ± 4.4	(39)	84.3[c] ± 5.1	(41)	0.3151

[a] Mean microvessel density per field (± standard error of the mean) based on CD31 immunohistochemical staining

[b] Number of fields analyzed; each sample set consisted of 3 animals per treatment group and 3 tissue sections analyzed for each animal

[c] In SSL-DXR treatment group, the increase in microvessel density from day 4 to day 7 was significant ($P<0.001$)

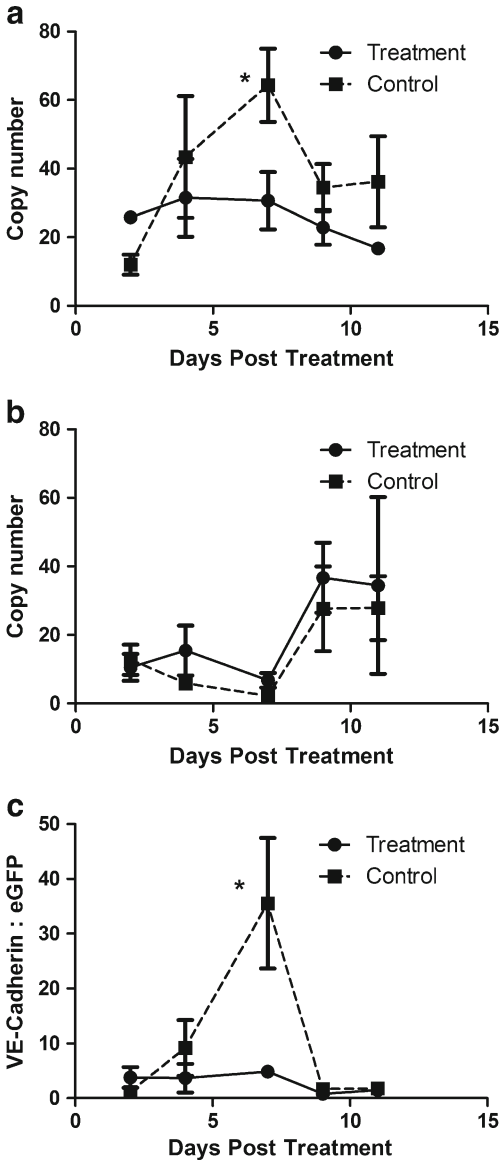

Fig. 5 Effect of SSL-DXR treatment on tumor content of vascular endothelial cells. Changes in tumor content of vascular endothelial cells or tumor cells mediated by a single dose of SSL-DXR were quantified by RT-PCR. On days 2, 4, 7, 9 and 11 after SSL-DXR treatment, groups of 3–5 animals treated with SSL-DXR or saline (controls) were sacrificed. Tumor burden (eGFP expression) and endothelial cell content (VE-cadherin, PECAM-1) were determined by qRT-PCR analysis. (**a**) VE-cadherin expression in tumor as a function of time after treatment with SSL-DXR (filled circles, solid line) or saline (control; filled squares, dashed line). Ordinate: data were normalized against multiple 'housekeeping' genes (Methods) and axis represents relative copy number. Treatment with a single dose of SSL-DXR abrogated the expansion of tumor endothelial cell content that was observed in control animals. The difference between control- and treated animals was significant on day 7 (*, $P < 0.05$). (**b**) Tumor cell density in harvested tissue samples based on 9L-eGFP cells included in tumor inoculum. Relative abundance of tumor cells increased as tumors grew more dense, excluding normal brain cells. (**c**) Vascular endothelium:tumor cell ratio in tissue samples. VE-cadherin expression (**a**) was normalized for each individual animal by its corresponding eGFP (tumor) content (**b**). The 7-fold suppression of VE-cadherin:eGFP ratio in SSL-DXR-treated animals relative to controls was statistically significant (*, $P < 0.05$). The data are the results of one complete, representative experiment. The experiment was performed twice, with at least 5 time points and n=3–5 animals per treatment group at each time point. The effect of SSL-DXR treatment to suppress peak endothelial cell expansion was statistically significant in both experiments (*, $P < 0.05$).

significance ($P < 0.05$) on day 7, thus corroborating the VE-cadherin data.

DISCUSSION

Novel drug carriers often progress through clinical trial based upon similarities between the encapsulated agent and the approved free drug. Doses and administration schedules usually reflect current clinical practice with the approved drug, and approval of the drug carrier formulation may hinge upon incremental improvements in toxicity profile, rather than improvements in efficacy that exceed what would be expected from dose escalation. Although expeditious, this strategy may de-emphasize or obscure novel, carrier-mediated alterations in pharmacology that arise from unique pharmacokinetic or biodistributional characteristics of the drug delivery system. Distinct toxicities of carrier-associated drugs have been observed clinically, such as the palmar-plantar erythrodysesthesia mediated by the nanoparticulate SSL-DXR formulation Doxil® (46), and this and other observations provide indirect clinical evidence that carrier-based formulations may exert unique pharmacological actions.

Previously we demonstrated that repeated weekly administrations of SSL-DXR in an intracranial brain tumor model prolonged survival, increased the tumor deposition of subsequent doses, and mediated progressive compromise of tumor vascular permeability (23–25). The changes observed in vascular permeability, which appear to result from establishment of an intra-tumor drug depot that is localized to the perivascular space, were not anticipated from prior preclinical or clinical reports. More recent investigations with encapsulated drugs such as irinotecan and vincristine demonstrate that nanoparticulate formulations containing drugs other than DXR can also exert effects upon tumor vasculature (30,31), and suggest that the nanoparticulate carrier system may play a generalizable role in modulating the observed pharmacology.

The sequence of events by which nanoparticulate drug carriers mediate vascular compromise is not well understood. Here we investigated the temporal responses of treatment-naïve tumors to a single dose of an SSL-DXR formulation that resembles Doxil®. DCE-MRI suggested that the initial effect of the SSL-DXR dose was a transient but significant reduction in tumor perfusion, which reached a nadir 3–4 days after treatment. This effect was tumor specific, as it was not observed in normal tissues such as contralateral brain or skeletal muscle. In parallel, qRT-PCR quantification of vascular endothelial cell markers demonstrated that a single SSL-

DXR dose abrogated the expansion of tumor vasculature occurring in control animals. Immunohistochemical analysis of tumor vascular content, employing CD31 as a marker, demonstrated that at the treatment-mediated nadir of tumor permeability/perfusion, a striking reduction was observed in tumor content of chaotic vascular elements. Instead, extensive organized CD31-positive structures were observed. These observations are consistent with 'vascular normalization' resulting from therapeutic targeting of tumor vasculature (47–49), in which tortuous, leaky, and immature tumor microvessels undergo remodeling to a 'normal' functionality and morphology. The observed reduction in microvessel density 3–4 days after SSL-DXR administration was statistically significant, and occurred in both the tumor core and peripheral invasive areas. Tumor deposition of fluorescent 85–110 nm SSL-DiI, which was employed as a nanoparticulate probe of vascular barrier compromise, was altered markedly by the single SSL-DXR dose. Whereas untreated animals showed sporadic but highly intense accretions of fluorescence in the tumor, SSL-DXR-treated animals lacked the intense accretions but appeared to contain a greater number of smaller fluorescent structures that had a morphology suggesting extravasation from underlying vascular structures without diffusion further into the tumor interstitium.

By 5–7 days after SSL-DXR treatment, tumors of treated and untreated animals converged to similar perfusion/permeability, based on DCE-MRI. Immunohistochemical analysis suggested that microvessel density in the treated animals had rebounded and was equal to control levels. Deposition of probe nanoparticles (SSL-DiI) on days 6–7 post-treatment was reduced significantly in the tumor core of both treated and control animals compared to day 3–4, despite the observed increase in microvessel density, suggesting a significant decline of vascular function as tumor progressed and cellularity increased.

Despite the fact that perfusion and permeability probes suggested a return to control values in SSL-DXR-treated animals by day 6–7 post-dose, qRT-PCR analysis showed that at day 7, tumor vascular endothelial cell content remained at a nadir in the SSL-DXR-treated animals. Thus the pharmacological effects of the single SSL-DXR dose upon tumor vasculature persisted for at least 7 days. Our previously-published data with this tumor model also support the conclusion that dynamic changes in the vasculature mediated by SSL-DXR were persistent: one week after dosing, DXR concentrations in tumors of SSL-DXR-treated animals were higher than the peak levels achieved immediately after bolus administration of an identical dose of free DXR (25). Vascular permeability continued to increase in SSL-DXR-treated animals beyond day 6–7 post-dose: tumor deposition of a second weekly SSL-DXR dose, which would peak on day 8–9 because of the long circulating lifetime of the SSL, was 2-fold higher than in treatment-naïve animals (25).

Two alternative hypotheses may explain the observed effects of SSL-DXR on tumor vascular status. The first is that extravasation of the initial SSL-DXR dose results in a persistent intratumor depot of drug that causes progressive tumor cell death, leading to collapse of the vasculature. The second is that extravasated liposomes fail to diffuse into the tumor because of their large radius of hydration, and the sustained drug release in close proximity to the vascular lumen is cytotoxic to the endothelial cells, leading to vascular collapse. The qRT-PCR data provided here would favor the second hypothesis: (i) the single SSL-DXR dose abolished a rapid expansion of vasculature that was observed in control tumors, under conditions in which (ii) tumor volume progression was not yet inhibited significantly by the SSL-DXR dose, based on qRT-PCR quantification of tumor cells, or tumor volume measurements by MR imaging, and (iii) the timeframe of maximum reduction in tumor vascular endothelial content was offset from the initial events, and corresponded to the timeframe in which rebound tumor vascular permeability was observed.

Additional mechanisms unique to the drug carrier system may contribute to the vascular compromise by SSL-DXR. The 2-fold reduction in tumor perfusion/permeability after 3–4 days, based on the AUC of Gd-DTPA in tumor (Fig. 2b), occurred 24-48 after peak SSL-DXR tumor deposition (25). A reduction in perfusion of that magnitude would reduce the clearance of extravasated liposomes (or released free drug) from the tumor immediately following peak deposition. Because back-diffusion to the systemic circulation may represent the most significant mechanism of clearance from tumor for most drugs (*e.g.,* as opposed to intra-tumor metabolism), a reduction in drug clearance after the majority of the overall tumor AUC was achieved could further intensify the effect of the intratumor SSL-DXR depot.

The temporal sequence of SSL-DXR effects upon tumor vascular permeability reported here may be difficult to discern in some tumor models. Deposition of SSL-DXR in advanced intracranial 9L tumors is just 0.02–0.04% of injected dose (25). In contrast, deposition of 5–13% of the injected SSL-DXR dose/g tumor was reported in mice bearing subcutaneous LS174T or B16 tumors (50), and deposition of 20% of the injected SSL-DXR dose/g was reported for subcutaneous Colon-26 tumors (51). The vascular permeability of *sc* tumors to nanoparticles may be unrealistically high in many tumor models. Notably, a comparison of *sc vs.* intracranial glioblastomas demonstrated a significantly lower k_{trans} in orthotopic tumors (31). In intracranial brain tumors, where the vascular barrier represents a significant hindrance to drug delivery, a two-fold increase in tumor drug deposition achieved with SSL-DXR, in parallel with a reduction in systemic drug clearance, could be highly significant therapeutically. However, in hypervascularized, high-permeability tumor models, such changes likely would be obscured.

Several prior reports are consistent with the observed effects of DXR-containing nanoparticles to reduce tumor perfusion/permeability. A rapid (≤30 min), tumor-selective reduction in microvessel flow, and a drastic decrease in tumor microvessel density (6–24 h post-dose), was observed when DXR was abruptly and rapidly released from temperature-triggered liposomes during hyperthermia (52). Here, the lower but sustained drug release rates from SSL-DXR also reduced tumor perfusion, but did so on a timescale that permitted the long-circulating SSL, which have a peak time of deposition of ≥24 h, to establish an intra-tumor drug depot before the perfusion that supports drug delivery was curtailed. Other investigations also report modulation of tumor vascular status by SSL-encapsulated drugs. In an *sc* tumor model, 6 weeks of treatment with a regimen of irinotecan-containing SSL reduced the vascular transfer constant k_{trans} and the tumor density of endothelial cells (30). However, the overall vasculature:tumor ratio was increased, and deposition of a second administered drug was increased as a result of the increased perfusion. Another report demonstrated that 3 different drugs encapsulated in SSL exert vasculature-modulating effects, and showed that after extended treatment of intracranial tumors, at highly efficacious doses, both vascular normalization and restoration of the tumor:blood barrier were observed in an intracranial brain tumor model (31). Thus with long-term treatment employing SSL-encapsulated agents, tumor properties may change in response to the accentuation of therapeutic effects in hyperpermeable regions of tumor. Together, these reports suggest that nanoparticulate drug carriers such as SSL initiate a dynamic sequence of effects, particularly upon tumor vasculature. Exploiting these effects would entail rational design of combination regimens, including non-standard administration patterns or regimens that are modified according to patient tumor response characteristics.

The key characteristics of nanoparticulate carriers required to exert tumor antivascular effects are likely to include: *i*) extended circulation time, so as to promote extravasation, *ii*) stable incorporation of the drug, so that the carrier is able to convey the drug to tumor, *iii*) an appropriate drug release rate, and *iv*) a particle diameter optimized for extravasation but retention in proximity to vascular elements. Previous studies have demonstrated the tradeoffs among hydrated radius of the carrier, tumor deposition of the drug/carrier complex, and the tissue penetration of the carrier-associated drug (13). Other studies demonstrated that the surface characteristics of SSL promote higher microvascular permeability compared to conventional liposomes that do not bear the PEG coating (53). Overall, the optimal values of the physicochemical characteristics required to achieve the observed antivascular effects of the drug:carrier complex are not well defined, but nonetheless these findings are relevant to other nanoparticulate drug formulations.

The sequelae that follow SSL-DXR administration have potentially important clinical ramifications. First, the administration of other agents in combination regimens could be less efficacious against tumor if administered during the transient period of reduction in tumor perfusion/permeability, conditions under which toxicity to critical normal tissues likely would be undiminished. This would have a deleterious impact on the therapeutic index. Clinically, non-invasive imaging could reveal whether a similar reduction of tumor perfusion occurs in patients administered SSL-DXR, as well as the duration of the effect. Second, the continuing intra-tumor effects of the SSL-DXR drug depot, which eventually increase tumor vascular permeability, could increase the efficacy of combination agents if administered within the appropriate time frame. Third, because antivascular effects observed with SSL-DXR are also exerted by mechanistically-distinct anti-cancer agents encapsulated in similar SSL (31), the emergence of pharmacological resistance may be combated by substituting an alternative SSL-drug complex, without loss of the concomitant effects upon the tumor vasculature.

CONCLUSIONS

The data presented demonstrate that a nanoparticulate drug/carrier complex that is similar to an FDA-approved product can exert vascular effects analogous to those observed with molecularly targeted antivascular agents. However, the pathophysiological mechanisms promoting SSL-DXR antivascular effects differ from those exerted by molecularly-targeted agents. Furthermore, the carrier-released drug appears to affect tumor vascular endothelial cells, which are not extensively mutated, in addition to the tumor cells. Therefore, treatment resistance to the antivascular effects of drugs in SSL would not be expected to arise from the same mechanisms responsible for the eventual failure of other vascular-targeted therapies (54,55). Finally, the effects of this drug/carrier complex upon tumor vascular permeability should be detectable by conventional clinical imaging modalities such as MRI. Thus, rationally-selected, patient-specific combination therapies could be designed to exploit what may be a transient yet significant treatment-mediated increase in tumor permeability mediated by nanoparticulate agents.

ACKNOWLEDGMENTS AND DISCLOSURES

We thank Dr. D. Brazeau (present address: University of New England) for advice and assistance in analyzing the qRT-PCR data, and Dr. Stelios Andreadis (University at Buffalo/SUNY) for the retroviral vector that was used to generate the 9L-eGFP cell line.

Support was provided by grant R01-CA107570 from the National Cancer Inst., National Institutes of Health, to RMS and the Comprehensive Cancer Center support grant (P30-CA016056) at Roswell Park. JY was supported by an unrestricted postdoctoral fellowship from the UB-Pfizer Strategic Alliance.

REFERENCES

1. Jemal A, Siegel R, Ward E, Hao Y, Xu J, Thun MJ. Cancer statistics, 2009. CA Cancer J Clin. 2009;59:225–49.
2. Ries LAG, Kosary CL, Hankey BF, Miller BA, Clegg L, Edwards BK. Surveillance epidemiology end result (SEER) cancer statistics review 1973–1996. Bethesda: National Cancer Institute; 1999.
3. Packer RJ. Brain tumors in children. Arch Neurol. 1999;56:421–5.
4. Fathallah-Shaykh H. New molecular strategies to cure brain tumors. Arch Neurol. 1999;56:449–53.
5. Demuth T, Rennert JL, Hoelzinger DB, Reavie LB, Nakada M, Beaudry C, *et al.* Glioma cells on the run—the migratory transcriptome of 10 human glioma cell lines. BMC Genomics. 2008;9:54.
6. Jain RK. Vascular and interstitial barriers to delivery of therapeutic agents in tumors. Cancer Metastasis Rev. 1990;9:253–66.
7. Jain RK. Haemodynamic and transport barriers to the treatment of solid tumours. Int J Radiat Biol. 1991;60:85–100.
8. Jang SH, Wientjes MG, Lu D, Au JL. Drug delivery and transport to solid tumors. Pharm Res. 2003;20:1337–50.
9. Tredan O, Galmarini CM, Patel K, Tannock IF. Drug resistance and the solid tumor microenvironment. J Natl Cancer Inst. 2007;99:1441–54.
10. Brem SS, Bierman PJ, Black P, Brem H, Chamberlain MC, Chiocca EA, *et al.* Central nervous system cancers. J Natl Compr Canc Netw. 2008;6:456–504.
11. Avgeropoulos NG, Batchelor TT. New treatment strategies for malignant gliomas. Oncologist. 1999;4:209–24.
12. Venturoli D, Rippe B. Ficoll and dextran *vs.* globular proteins as probes for testing glomerular permselectivity: effects of molecular size, shape, charge, and deformability. Am J Physiol Renal Physiol. 2005;288:F605–13.
13. Dreher MR, Liu W, Michelich CR, Dewhirst MW, Yuan F, Chilkoti A. Tumor vascular permeability, accumulation, and penetration of macromolecular drug carriers. J Natl Cancer Inst. 2006;98:335–44.
14. Drummond DC, Meyer O, Hong K, Kirpotin DB, Papahadjopoulos D. Optimizing liposomes for delivery of chemotherapeutic agents to solid tumors. Pharmacol Rev. 1999;51:691–743.
15. Gabizon A, Papahadjopoulos D. Liposome formulations with prolonged circulation time in blood and enhanced uptake by tumors. Proc Natl Acad Sci USA. 1988;85:6949–53.
16. Gabizon A, Shiota R, Papahadjopoulos D. Pharmacokinetics and tissue distribution of doxorubicin encapsulated in stable liposomes with long circulation times. J Natl Canc Inst. 1989;81:1484–8.
17. Allen TM, Chonn A. Large unilamellar liposomes with low uptake into the reticuloendothelial system. FEBS Lett. 1987;223:42–6.
18. Davis ME, Chen ZG, Shin DM. Nanoparticle therapeutics: an emerging treatment modality for cancer. Nat Rev Drug Discov. 2008;7:771–82.
19. Torchilin VP. Targeted pharmaceutical nanocarriers for cancer therapy and imaging. AAPS J. 2007;9:E128–47.
20. Li SD, Huang L. Pharmacokinetics and biodistribution of nanoparticles. Mol Pharm. 2008;5:496–504.
21. Muggia FM. Liposomal encapsulated anthracyclines: new therapeutic horizons. Curr Oncol Rep. 2001;3:156–62.
22. Gabizon AA. Pegylated liposomal doxorubicin: metamorphosis of an old drug into a new form of chemotherapy. Canc Investig. 2001;19:424–36.
23. Zhou R, Mazurchuk R, Straubinger RM. Antivasculature effects of doxorubicin-containing liposomes in an intracranial rat brain tumor model. Cancer Res. 2002;62:2561–6.
24. Sharma US, Sharma A, Chau RI, Straubinger RM. Liposome-mediated therapy of intracranial brain tumors in a rat model. Pharm Res. 1997;14:992–8.
25. Arnold RD, Mager DE, Slack JE, Straubinger RM. Effect of repetitive administration of doxorubicin-containing liposomes on plasma pharmacokinetics and drug biodistribution in a rat brain tumor model. Clin Cancer Res. 2005;11:8856–65.
26. Mayer LD, Bally MB, Cullis PR. Uptake of adriamycin into large unilamellar vesicles in response to a pH gradient. Biochim Biophys Acta. 1986;857:123–6.
27. Haran G, Cohen R, Bar LK, Barenholz Y. Transmembrane ammonium sulfate gradients in liposomes produce efficient and stable entrapment of amphipathic weak bases. Biochim Biophys Acta. 1993;1151:201–15.
28. Lasic DD, Frederik PM, Stuart MC, Barenholz Y, McIntosh TJ. Gelation of liposome interior. A novel method for drug encapsulation. FEBS Lett. 1992;312:255–8.
29. Tailor TD, Hanna G, Yarmolenko PS, Dreher MR, Betof AS, Nixon AB, *et al.* Effect of pazopanib on tumor microenvironment and liposome delivery. Mol Cancer Ther. 2010;9:1798–808.
30. Baker JH, Lam J, Kyle AH, Sy J, Oliver T, Co SJ, *et al.* Irinophore C, a novel nanoformulation of irinotecan, alters tumor vascular function and enhances the distribution of 5-fluorouracil and doxorubicin. Clin Cancer Res. 2008;14:7260–71.
31. Verreault M, Strutt D, Masin D, Anantha M, Yung A, Kozlowski P, *et al.* Vascular normalization in orthotopic glioblastoma following intravenous treatment with lipid-based nanoparticulate formulations of irinotecan (Irinophore C), doxorubicin (Caelyx) or vincristine. BMC Cancer. 2011;11:124.
32. Weidensteiner C, Rausch M, McSheehy PM, Allegrini PR. Quantitative dynamic contrast-enhanced MRI in tumor-bearing rats and mice with inversion recovery TrueFISP and two contrast agents at 4.7 T. J Magn Reson Imaging. 2006;24:646–56.
33. Choyke PL, Dwyer AJ, Knopp MV. Functional tumor imaging with dynamic contrast-enhanced magnetic resonance imaging. J Magn Reson Imaging. 2003;17:509–20.
34. Trummer BJ, Iyer VS, Balu-Iyer SV, O'Connor R, Straubinger RM. Physicochemical properties of EGF receptor inhibitors and development of a nanoliposomal formulation of gefitinib. Journal of Pharmaceutical Sciences. 2012;in press.
35. Oh Y-K, Nix DE, Straubinger RM. Formulation and efficacy of liposome-encapsulated antibiotics for therapy of intracellular M. avium infection. Antimicrob Agents Chemother. 1995;39:2104–11.
36. Madden TD, Harrigan PR, Tai LC, Bally MB, Mayer LD, Redelmeier TE, *et al.* The accumulation of drugs within large unilamellar vesicles exhibiting a proton gradient: a survey. Chem Phys Lipids. 1990;53:37–46.
37. Harrigan PR, Wong KF, Redelmeier TE, Wheeler JJ, Cullis PR. Accumulation of doxorubicin and other lipophilic amines into large unilamellar vesicles in response to transmembrane pH-gradients. Biochim Biophys Acta. 1993;1149:329–48.
38. Li X, Hirsh DJ, Cabral-Lilly D, Zirkel A, Gruner SM, Janoff AS, *et al.* Doxorubicin physical state in solution and inside liposomes loaded via a pH gradient. Biochim Biophys Acta. 1998;1415:23–40.
39. Bartlett GR. Phosphorus assay in column chromatography. J Biol Chem. 1959;234:466–8.

40. Ghods AJ, Irvin D, Liu G, Yuan X, Abdulkadir IR, Tunici P, *et al.* Spheres isolated from 9L gliosarcoma rat cell line possess chemoresistant and aggressive cancer stem-like cells. Stem Cells. 2007;25:1645–53.
41. Schmitt P, Griswold MA, Jakob PM, Kotas M, Gulani V, Flentje M, *et al.* Inversion recovery TrueFISP: quantification of T(1), T(2), and spin density. Magn Reson Med. 2004;51:661–7.
42. Shih SC, Robinson GS, Perruzzi CA, Calvo A, Desai K, Green JE, *et al.* Molecular profiling of angiogenesis markers. Am J Pathol. 2002;161:35–41.
43. Vandesompele J, De Preter K, Pattyn F, Poppe B, Van Roy N, De Paepe A, *et al.* Accurate normalization of real-time quantitative RT-PCR data by geometric averaging of multiple internal control genes. Genome Biol. 2002;3:RESEARCH0034.
44. Meers P, Ali S, Erukulla R, Janoff AS. Novel inner monolayer fusion assays reveal differential monolayer mixing associated with cation-dependent membrane fusion. Biochim Biophys Acta. 2000;1467:227–43.
45. Saito R, Bringas JR, McKnight TR, Wendland MF, Mamot C, Drummond DC, *et al.* Distribution of liposomes into brain and rat brain tumor models by convection-enhanced delivery monitored with magnetic resonance imaging. Cancer Res. 2004;64:2572–9.
46. Lyass O, Uziely B, Ben-Yosef R, Tzemach D, Heshing NI, Lotem M, *et al.* Correlation of toxicity with pharmacokinetics of pegylated liposomal doxorubicin (Doxil) in metastatic breast carcinoma. Cancer. 2000;89:1037–47.
47. Jain RK. Normalization of tumor vasculature: an emerging concept in antiangiogenic therapy. Science. 2005;307:58–62.
48. Batchelor TT, Sorensen AG, di Tomaso E, Zhang WT, Duda DG, Cohen KS, *et al.* AZD2171, a pan-VEGF receptor tyrosine kinase inhibitor, normalizes tumor vasculature and alleviates edema in glioblastoma patients. Cancer Cell. 2007;11:83–95.
49. Escorcia FE, Henke E, McDevitt MR, Villa CH, Smith-Jones P, Blasberg RG, *et al.* Selective killing of tumor neovasculature paradoxically improves chemotherapy delivery to tumors. Cancer Res. 2010;70:9277–86.
50. Gabizon A, Price DC, Huberty J, Bresalier RS, Papahadjopoulos D. Effect of liposome composition and other factors on the targeting of liposomes to experimental tumors: biodistribution and imaging studies. Cancer Res. 1990;50:6371–8.
51. Huang S, Lee K-D, Hong K, Friend D, Papahadjopoulos D. Microscopic localization of sterically-stabilized liposomes in colon-carcinoma-bearing mice. Cancer Res. 1992;52:5135–43.
52. Chen Q, Tong S, Dewhirst MW, Yuan F. Targeting tumor microvessels using doxorubicin encapsulated in a novel thermosensitive liposome. Mol Cancer Ther. 2004;3:1311–7.
53. Wu N, Da D, Rudoll T, Needham D, Whorton A, Dewhirst M. Increased microvascular permeability contributes to preferential accumulation of Stealth™ liposomes in tumor tissue. Cancer Res. 1993;53:3766–70.
54. Paez-Ribes M, Allen E, Hudock J, Takeda T, Okuyama H, Vinals F, *et al.* Antiangiogenic therapy elicits malignant progression of tumors to increased local invasion and distant metastasis. Cancer Cell. 2009;15:220–31.
55. Ebos JM, Lee CR, Cruz-Munoz W, Bjarnason GA, Christensen JG, Kerbel RS. Accelerated metastasis after short-term treatment with a potent inhibitor of tumor angiogenesis. Cancer Cell. 2009;15:232–9.